

# Localized X-ray photoelectron impedance spectroscopy (LoXPIS) for capturing charge dynamics of an ionic liquid electrolyte within an energy storage device

Mustafa Başaran,<sup>a</sup> Erdinc Oz,<sup>b</sup> Said Ergoktas,<sup>c</sup> Coskun Kocabas,<sup>c</sup> Burak Ulgut,<sup>b</sup> Askin Kocabas<sup>\*a</sup> and Sefik Suzer<sup>id</sup><sup>\*b</sup>

Received 29th November 2021, Accepted 12th January 2022

DOI: 10.1039/d1fd00102g

Many electrochemical devices are based on the fundamental process of ion migration and accumulation on surfaces. Complex interplay of molecular properties of ions and device dimensions control the entire process and define the overall dynamics of the system. Particularly, for ionic liquid-based electrolytes it is often not clear which property, and to what extent, contributes to the overall performance of the device. Herein we use X-ray photoelectron spectroscopy (XPS) while the device is under electrical bias. Such a procedure reveals localized electrical potential developments, through binding energy shifts of the atomic core levels, in a chemically specific fashion. Combining it with square-wave AC modulation, the information can also be extended to time domain, and we investigate devices configured as a coplanar capacitor, with an ionic liquid as the electrolyte, in macro-dimensions. Our analysis reveals that a nonlinear voltage profile across the device emerges from spatially non-uniform electrical double layer formation on electrode surfaces. Interestingly the coplanar capacitor has an extremely slow time response which is particularly controlled by IL film thickness. XPS measurements can capture the ion dynamics in the tens of seconds to microseconds range, and reveal that ionic motion is all over the device, including on metallic electrode regions. This behavior can only be attributed to motion in more than one dimension. The ion dynamics can also be faithfully simulated by using a modified PNP equation, taking into account steric effects, and device dimensions. XPS measurements on two devices with different dimensions corroborated and validated the simulation results. The present results propose a new experimental approach and provide new insights into the dynamics of ions across electrochemical devices.

<sup>a</sup>Department of Physics, Koc University, Istanbul, 34450, Turkey. E-mail: akocabas@ku.edu.tr

<sup>b</sup>Department of Chemistry, Bilkent University, Ankara, 06800, Turkey. E-mail: suzer@fen.bilkent.edu.tr

<sup>c</sup>Department of Materials, University of Manchester, Manchester M13 9PL, UK

## Introduction

Motion of ions within electrified electrodes that have liquid electrolytes in between is the most important process controlling the performance of many electrochemical systems, spanning a wide range of micro- and macro-devices, used for investigation of bio-systems,<sup>1,2</sup> batteries,<sup>3</sup> fuel-cells,<sup>4</sup> solar-cells<sup>5</sup> and super-capacitors,<sup>6</sup> *etc.* Ionic liquids have recently been added to the conventional list of electrolytes, and have quickly assumed a promising role, due to their convenient physical and chemical properties, such as low-volatility, high conductivity, larger operating potential window, and low toxicity.<sup>7–10</sup> The most important phenomenon affecting the ionic motion or transport in all of these systems has long been advocated to be the formation of the Electrical Double-Layer (EDL) for both faradaic and non-faradaic processes, since ions at the interface of the polarized/charged surfaces can and do rearrange to screen this charge.<sup>11</sup> The resulting concentration and, therefore, the electrical potential profile at the electrode/electrolyte interface further triggers a multitude of processes controlling the kinetics and thermodynamics of the electrochemical systems.<sup>12</sup> Therefore, investigation of static and dynamic properties of the EDL has been a focus both experimentally and theoretically dating back to Helmholtz approaching 17 decades ago.<sup>13</sup>

Recent progress has shed further light on the time dependency, particularly the nonlinear response of the thin double layer in a parallel plate configuration, where Bazant *et al.* identified different time scales controlled by geometric and ionic diffusion properties of the chemical make-up within such devices.<sup>14–16</sup> Most of these approaches have been developed and tested for small electrical potentials and relatively dilute aqueous solutions, while extension to higher voltages and highly concentrated electrolytes, as in the case of ionic liquids, still remains a challenging task due to the high interaction energy and long-range coulombic forces. Accordingly, the same group had modified their theoretical approaches and developed a comprehensive model (Bazant–Storey–Kornyshev, aka BSK theory) including steric interactions, overcrowding and under-screening dynamics of RTILs.<sup>17–19</sup> Alternatively, the pattern formation frameworks particularly mesoscale phase separation principles have been recently implemented to reveal the clustering behavior of ILs.<sup>20–22</sup>

All of these new concepts have also been tested using electro-chemical,<sup>23–27</sup> microscopic,<sup>28–30</sup> terahertz imaging,<sup>31</sup> and X-ray scattering techniques,<sup>32,33</sup> strongly guided and/or corroborated by modeling/simulation studies.<sup>34,35</sup> Use of electro-chemical force microscopy has given intriguing new input into the dynamics of charge screening at the solid–aqueous interfaces by identifying multiple time constants and relatively larger length scales of up to 10 microns.<sup>36,37</sup> But again, such distances are still too small to represent real-life electrochemical devices, moreover, information not only at the interfaces but in regions covering the entire device are needed.

Recent findings clearly point out that dynamics of the charging processes in devices with ionic liquids as electrolytes differ widely from conventional ones exhibiting multiple time and length scales, spanning from very fast, Debye-layer charging ( $10^{-9}$  s) to ultra-slow, bifurcation-like ( $10^4$  s) processes under static or time-varying electrical stresses.<sup>38–45</sup> Although these methods illuminate the

electrostatic phenomena at the interface, the link to the underlying physics/chemistry is missing. Deeper understanding of the detailed charge diffusion dynamics and evolution of double layer formation across millimeter-large device structures is still elusive. In order to give a different perspective, we combine X-ray photoelectron spectroscopy (XPS) with AC modulation and computational models, covering steric effects and large-scale device configurations.

XPS is a favorable chemical analysis tool and gives quantitative information with high surface sensitivity, but only with a limited spatial resolution, on orders of 50–100 microns for the lab-based instruments. On the other hand, an underutilized advantage of XPS is the capability to faithfully reflect the local electrical potential profiles, vital for further advancement of various applications of electrochemical systems. Under an electrical bias, core level photoelectrons measured by XPS undergo binding energy shifts which reflect the local potential ( $V$ ) on investigated surfaces in a chemically specific fashion. Here, the limit of the energy sensitivity of the common lab-based instruments is about 100 meV, and the technique is also relatively non-invasive. This is related to the expected  $IR$  drop due to the low currents related to the photoelectron emission process on orders of  $\sim 1$  nA, which translates to a negligibly small energy shift of  $\sim 1$  meV for an ionic liquid film having  $\sim 1$  M $\Omega$  resistance, and not measurable by XPS. In one of the first studies of ionic liquids, a drop of ionic liquid was placed on an inclined electrode.<sup>46</sup> Their experimental set-up enabled formation of a liquid film thin enough to probe the IL/electrode interface such that the authors were able to follow the EDL processes by tracing the shifts in the core-level binding energies under external potential bias. Whereas, application of DC potentials during XPS data acquisition provides steady state information, our group has previously shown that AC excitation is indispensable for investigation of the dynamics of electrical potential developments.<sup>47–52</sup>

In this study, we report on using XPS to directly probe certain features of the diffuse charge dynamics of a sample in the form of a coplanar-plate capacitor geometry, having an IL as the electrolyte, while imposing a square-wave (AC) potential excitation with frequencies ranging from mHz to kHz at room temperature. Note that for the commonly used parallel plate capacitor, the probing XPS beam would not have direct access to the electrical double layer. Using a coplanar capacitor configuration instead, we have the opportunity to spatially extend the beam and probe the effects of screening the applied potential through ion movement across a large electrolyte medium, since the ionic motion materializes in all regions of the device. Square-wave, rather than conventional electrochemical sine-wave modulation is preferred, since it causes almost no distortion of the XPS peaks.

Supported with numerical simulations, particularly by taking into account the 2-dimensional nature of ionic motion, our analyses consist of XPS data gathering in the forms of areal and line scans at different but constant frequencies for giving spatial information throughout the extended length scales.<sup>47,48,53</sup> Our approach provides new insights into potential developments, particularly on spatial charge dynamics on devices, at the positions they occur. Mapping the 2-D spatiotemporal dynamics of IL is an important and timely approach to tap into the complex non-equilibrium and pattern formation phenomena which have attracted significant scientific interest recently.<sup>21,22,54–56</sup>

## Experimental

*N,N*-Diethyl-*N*-methyl-*N*-(2-methoxyethyl)ammonium bis(trifluoromethanesulfonyl)imide (DEME-TFSI) was purchased from Sigma-Aldrich and used without any purification. DEME-TFSI is chosen as the ionic liquid medium, since it has a relatively large electro-chemical window, and has a strong F 1s signal (6 F atoms per anion) for better data processing. The coplanar capacitor device configuration used in this study consists of two Au electrodes deposited onto a porous polyethylene membrane (PEM, from Gelon LIB), which are used as the source and the drain electrodes, and a 5  $\mu$ L ionic liquid (DEME-TFSI) is soaked into the uncovered membrane in between, acting as a continuous liquid film as the electrolyte medium. One of the electrodes is used as a working electrode to apply the external bias while the other one, the counter electrode is always kept at ground potential.

A Thermo Fisher K-alpha X-ray photoelectron spectrometer with monochromatized X-rays of 1486.6 eV is used for all XPS measurements. Core level spectra were collected using 50 eV analyzer pass energy, but for time-resolved XPS measurements, the fast data gathering, the snapshot mode with 150 eV pass

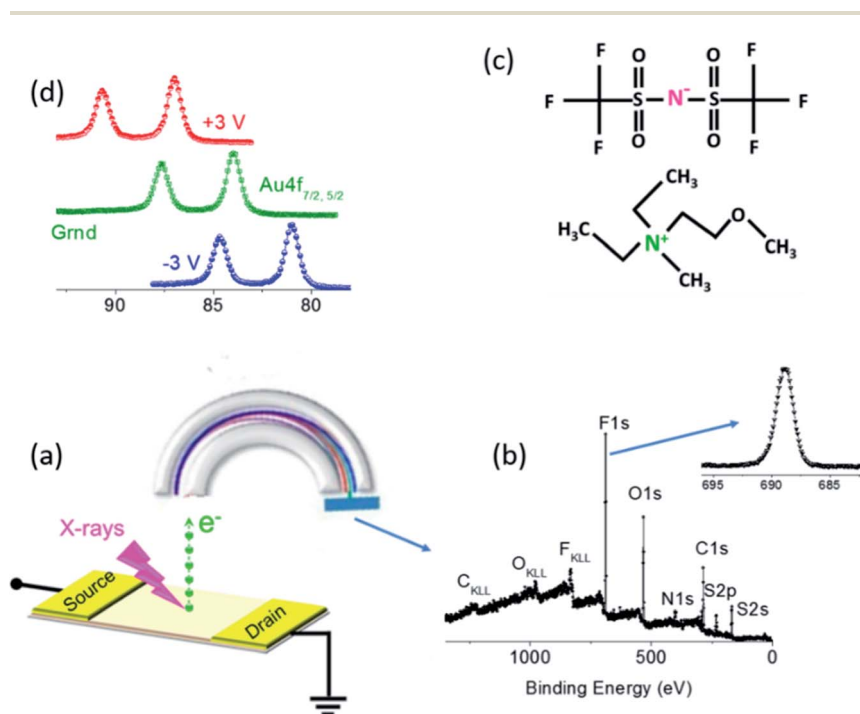


Fig. 1 (a) Schematics of the co-planar capacitor for probing the dynamics of the charging of the ionic liquid medium by the XPS probe beam, under *operando* conditions, where both current and peak positions are recorded simultaneously. The function generator is connected to the source electrode to impose a DC, or an AC (SQW), excitation with a fixed or variable frequency. (b) Survey XP spectrum of the IL and F 1s region representative of the anion. (c) Chemical formula of the IL. (d) Au 4f XP spectra, recorded at the source electrode and under  $-3$ ,  $0$ , and  $+3$  V DC bias.

energy is used instead of the scanning mode. X-Ray spot size is set to 50  $\mu\text{m}$  for line scan and 100  $\mu\text{m}$  for single point measurements. Pressure in the analyzing chamber is always kept under  $10^{-8}$  mbar. Fitting procedure is performed using the Advantage software equipped with the instrument. All the fits reported in this work have been carried out using a symmetrical Gaussian/Lorentzian product function with ratios of 30/70 after Shirley background subtraction. A schematic representation of the device with the ionic liquid and the gold electrodes is shown in Fig. 1(a). An XP survey spectrum of the IL, together with a scanned spectrum of the F 1s region, is depicted in Fig. 1(b). The chemical formula of the IL is displayed in Fig. 1(c). Fig. 1(d) shows XP spectra of the Au 4f spin-orbit doublet, recorded at the source electrode and under  $-3$ ,  $0$ , and  $+3$  V DC bias.

## Simulations

To gain a more quantitative representation of charge dynamics, we performed Finite Element Method (FEM) simulations based on Poisson–Nernst–Planck (PNP) equations.<sup>21,22</sup> Conventional PNP equations can only capture the drift-diffusion dynamics of dilute electrolytes. However, in IL due to finite size effects of ions, these equations require precise modifications to take into account the essential steric effects. The other important feature we must also consider is the diffusion process of ionic liquids. An IL is a solvent-free, molten salt and it maintains uniform total ion density ( $p + n = 2c_0$ ). Unlike dilute ions in a solvent, due to this constraint, diffusion dynamics of an IL are driven by the inter-diffusion process which can be implemented by following the Onsager framework ( $\mathbf{J} \sim pn\nabla(\mu)$ ), where  $\mu$  is the chemical potential.<sup>21,22</sup>

Several models have recently been developed for RTILs. Specifically, we restrict ourselves to a Chan–Hillard–Poisson type framework to include all these steric effects, coulombic interactions and the Onsager diffusion process.<sup>20–22</sup> We used COMSOL Multiphysics for modeling. Following Gavish and Yochelis,<sup>20</sup> the free energy can be written as

$$\mathcal{F} = \int k_{\text{B}}T [p \ln p + n \ln n] + \left[ q(p - n)\phi - \frac{\epsilon}{2} |\nabla\phi|^2 \right] + \frac{1}{c_0} \left[ \frac{\beta np}{4} + \frac{\epsilon_0 \kappa^2}{4} (|\nabla p|^2 + |\nabla n|^2) \right]$$

$p$  and  $n$  are cation and anion molar concentrations,  $c_0 = 3.3$  M is the initial bulk ion concentration and  $\phi$  is the electric potential. Further, the modified Poisson–Nernst–Planck equations and the corresponding currents are given below;

$$\frac{\partial p}{\partial t} = -\nabla \cdot \mathbf{J}$$

$$\mathbf{J} = \frac{Dpn}{k_{\text{B}}Tc_0} \nabla \left( k_{\text{B}}T \ln \frac{p}{n} + 2ze\phi - \frac{\beta(c_{\text{ref}} - p)}{2c_0} - \epsilon_0 \kappa^2 \nabla^2 p \right)$$

$$\epsilon \nabla^2 \phi = -q(p - n)$$

where,  $D_i \cong 1 \times 10^{-11} \text{ m}^2 \text{ s}^{-1}$  is the isotropic diffusion coefficient,<sup>56</sup>  $q$  is the elementary charge and  $\epsilon \sim 20$  is the dielectric constant of the IL.<sup>57</sup> We assume an equal ion diameter  $a \cong 0.4\text{--}0.6 \text{ nm}$  which sets the maximum ion concentration to  $2c_0 \cong 6.6 \text{ M}$  through the ionic steric interactions.

## Results and discussion

### (I) XPS measurements

**(I-a) Measuring the localized equilibrium voltage distributions.** The Au  $4f_{7/2}$  peak has a binding energy of 84.0 eV when the system is grounded but shifts to 87.0 and 81.0 eV when biased with +3 and  $-3 \text{ V}$ , respectively, and no corresponding shifts are observable for the same spectrum recorded on the grounded drain electrode. When both of the electrodes are grounded, the F  $1s$  peak appears at the tabulated binding energy position of 688.5 eV, and is expected to shift to a higher (lower) position under positive (negative) bias respectively. However, contrary to the trivial 3.0 eV shifts of the electrode Au  $4f$  peaks [see Fig. 1(d), 2(a) and (c)], the F  $1s$  peak undergoes smaller shifts due to screening of the electrode potential, hence gives pertinent information both under DC and AC actuations, related to static and dynamic screening, respectively, operative within the entire probed system. Such a situation is shown in Fig. 2, for our coplanar capacitor,

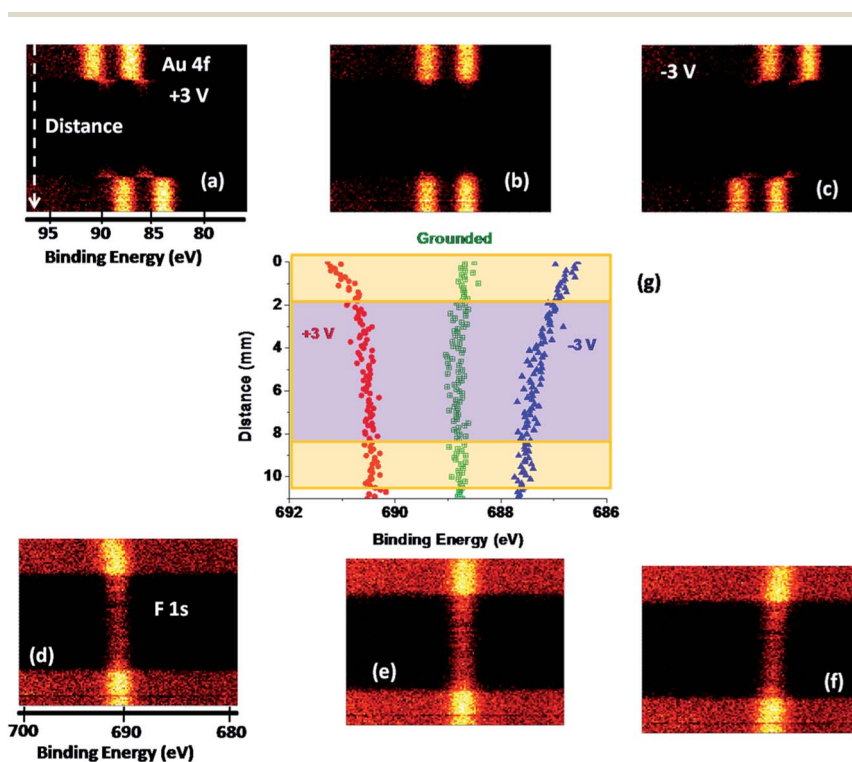


Fig. 2 Recorded line-scan XP spectra under +3, 0 and  $-3 \text{ V}$  DC bias, respectively. (a)–(c) Au  $4f$  region representative of the metal electrodes. (d)–(f) F  $1s$  region representative of the IL. (g) Extracted F  $1s$  binding energy variations.

where line scan spectra of the Au 4f and also F 1s peaks are displayed along the central line of the capacitor.

The line starts on the source electrode, which is  $\sim 2$  mm wide and continues along the entire  $\sim 6$  mm electrolyte film and ends after spanning the grounded electrode. Note that the electrodes are also partially covered with a thin layer of the liquid electrolyte, since the F 1s signal is also measurable in that region. Screening effects at the quasi-steady-state ( $>500$  s) are readily seen, as exemplified by the measured F 1s peak as a function of the position of the probe beam on and across the electrodes, in Fig. 2(d) and (f). The F 1s peak undergoes shifts less than the applied voltage, due to the effective screening through the double layer formation on the electrodes, hence can be used as the reflection of the local electrical potential within the device.

**(I-b) Measuring the temporal and localized voltage distributions.** To capture the temporal variations across the device, we recorded the F 1s region in the snapshot mode with 1 second time-intervals at a low frequency of 10 mHz (100 spectra in one cycle), as depicted in Fig. 3, at the three positions indicated.

It is seen from Fig. 3(a) and (e), when the positive cycle begins, the F 1s shifts instantaneously by almost +3 eV ( $688.5 + 3 = 691.5$  eV) and gets shifted down as the screening takes place, with an approximate time constant of 4 seconds. During the negative cycle [Fig. 3(a) and (f)], the corresponding value is 685.5 eV and the time constant is more than twice that of the positive one. Moreover, response of the F 1s on the other electrode is quite different. In addition, there are

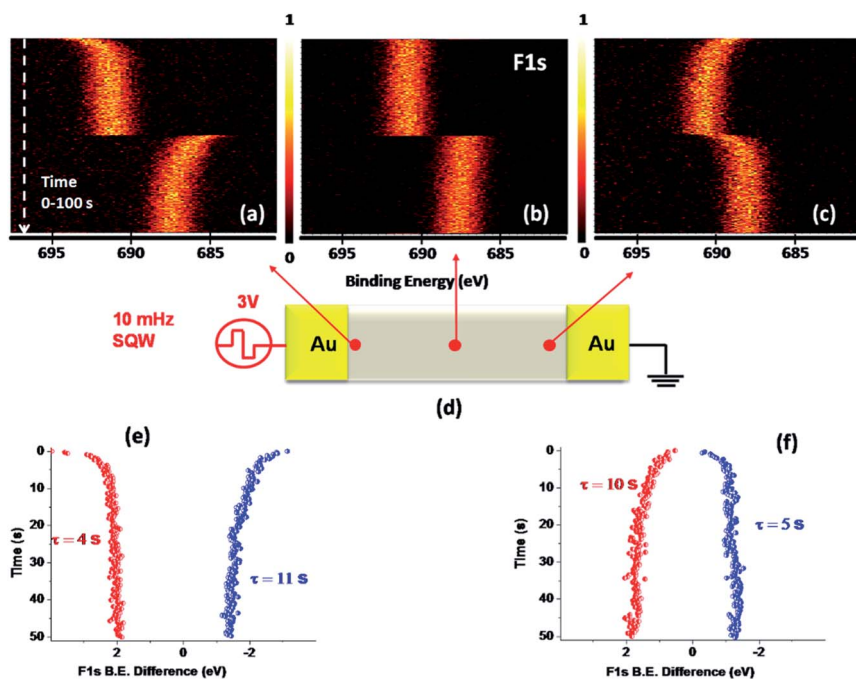


Fig. 3 (a)–(c) F 1s XP spectra of the IL recorded in the snap-shot mode at three different positions of the capacitor. (d) Schematics of the device. (e) and (f) Variation of the differences in the F 1s B.E. as a function of time, extracted from (a) and (c), respectively.

no measurable temporal shifts in the F 1s peak position in the middle of the device, in perfect harmony with the near-electrode measurements.

The most logical hypothesis explaining this observation is that the varying and transient voltage levels across the device are gradually approaching to the equilibrium distribution ( $\sim 1.5$  V). These results indicate that the response time of the device is slow enough to observe the detailed voltage transitions across the capacitor using XPS measurements. Note in passing that ionic motion is evident all over the device, and is controlled presumably by a combination of different electrochemical processes, and can easily be captured by XPS measurements.

These results bring out several interesting features which differ from those of a simple parallel plate electrolytic capacitor with blocking metal electrodes, such as: (i) very slow electrical response time, (ii) presence of asymmetric equilibrium voltage distribution, (iii) non-uniform and nonconforming (due to effective screening) electrical potential distribution on the surface of IL moieties and across the metal electrodes. Naively, we can claim that these observations are originating from the interplay of steric effects, geometrical constraints and the IL's droplet coverage of the large gold electrodes. Using the computational model we will further focus on these distinct features to reveal the detailed factors controlling these responses.

**(I-c) Measuring the transient and localized voltage distributions.** As a next step we focused on frequency response of our coplanar capacitor. We have been using a procedure to extract time-dependent variations of localized electrical potential developments, by recording XP spectra under square-wave AC modulation, which introduces a controllable time-window while causing minimum distortion to the

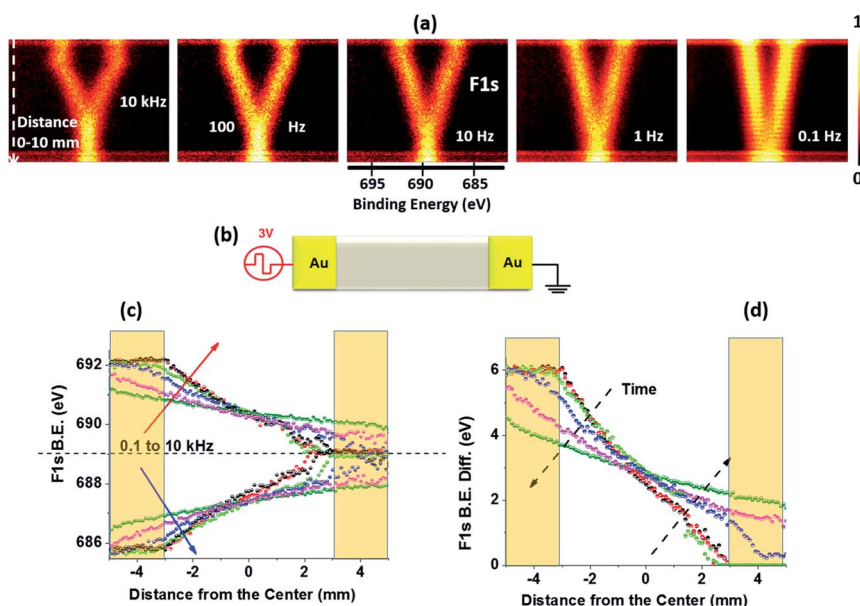


Fig. 4 (a) XPS spectra of the F 1s region of the IL across the coplanar capacitor, recorded under various 3 V SQW excitations. (b) Schematics of the device. (c) Extracted BEs, and (d) their differences as a function of the distance across the coplanar-capacitor.

line-shape as depicted in Fig. 4(a). The format of the spectra is in the forms of line-scans along the central line of the capacitor, and is similar to those given in Fig. 2. However, now both the positive and the negative cycles are depicted simultaneously, spanning a wide frequency range of 5 decades (0.1 Hz to 10 kHz), reflecting the time-dependent local potential developments along the entire capacitor.

**(I-d) Transient and localized voltage distributions in two different devices.** As was mentioned in the Introduction section, for a parallel plate capacitor, Bazant, through simulations predicted three time scales, which are:  $\tau_D = \lambda_d^2/D$ ,  $\tau_c = \lambda_d L/D$  and  $\tau_L = L^2/D$ , where  $\lambda_d$  is the Debye length,  $2L$  is the distance between electrodes and  $D$  is the diffusion constant. These are the time constants associated with local charge redistribution (EDL), diffusion across the cell, and the diffuse-charge dynamics, respectively. To check the validity of this prediction, we have also carried out similar measurements on another co-planar capacitor device which has only half of the IL channel width of  $2L = 3$  mm. The results are depicted in Fig. 5, together with the first device ( $2L = 6$  mm) reported in previous sections, yielding more or less the same local potential screening, except for a faster response, probably attributable to the higher electrical field imposed. The largest potential screenings are measured right near the two interfaces of the metal electrodes with the IL film, but screening throughout the metal electrodes is also significant. We can obtain information regarding: (i) the quantity of the screened charges, and also (ii) their dynamics, using the extracted screened potentials ( $-2.4$  and  $-1.9$  V for these two devices, both in 10 seconds).

The screening potential developed between the center of the device ( $L = 0$ ) and the interface ( $L = 3$  mm) can in turn be related to the ionic charges through the following equation:<sup>11</sup>

$$q = 4\pi\epsilon\epsilon_0 L \times \Phi = 4\pi \times 20 \times 8.85 \times 10^{-12} \frac{F}{m} \times 0.003 \text{ m} \times (2.4 \text{ V}) = 6 \times 10^{-13} \text{ C}$$

where a dielectric constant of 20 is used for the IL.<sup>57</sup> This formula tells us that an ion concentration difference of  $\sim 4 \times 10^6$  develops within 10 seconds (between 0.1 Hz and 10 kHz).

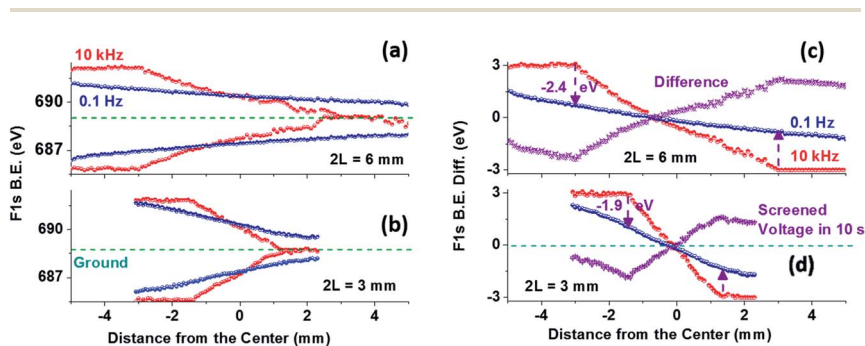


Fig. 5 Measured binding energy of the F 1s peak recorded with 10 kHz and 0.1 Hz 3 V SQW modulation across the two coplanar capacitors: (a)  $2L = 6$  mm and (b)  $2L = 3$  mm, respectively. The corresponding and extracted B.E. differences between the two frequencies together with effective screened local electrical potentials for the two devices are given in (c) and (d).

If we use the diffusion constant of  $5 \times 10^{-11} \text{ m}^2 \text{ s}^{-1}$ , we would get a diffusion length of only  $[(5 \times 10^{-11} \text{ m}^2 \text{ s}^{-1} \times 10 \text{ s})^{0.5} = ] 0.02 \text{ mm}$  for the time interval of 10 s. Alternatively, we can use the viscosity coefficient of the IL ( $\eta = \sim 50 \text{ cP}$ ),<sup>58</sup> under the applied potential of 3 V to estimate the drift velocity ( $\bar{u}$ ) using the following formula:<sup>11</sup>

$$\bar{u} = E \times e/6\pi\eta r = (2.4 \text{ V}/0.003 \text{ m}) \times (1.6 \times 10^{-19} \text{ C})/(6\pi \times 50 \text{ cP} \times 0.2 \text{ nm}) = 7 \times 10^{-6} \text{ m s}^{-1}$$

where,  $r$  is the ion radius ( $\sim 0.2 \text{ nm}$ ). This formula yields  $\sim 0.07 \text{ mm}$  for the time interval of 10 s. Both of these two naive approaches yield more than 2 orders of magnitude smaller ion movements when compared with our XPS measurements. Hence, other experimental and/or geometrical parameters must be in effect to explain the results.

## (II) Simulations

### (II-a) Numerical simulations of charge dynamics of a parallel plate capacitor.

To validate the numerical simulations, we first focused on the 1D parallel plate capacitor configuration. As an initial step we assessed the time response of the capacitor and contribution of steric effects and clustering dynamics to this charging process. We transiently applied a voltage step (1 V) to one electrode and grounded the other one. Fig. 4 summarizes the time responses of the IL based capacitor. Although the initial voltage distribution across the capacitor is linear between 0 to 1 V, at the steady state, through the two equivalent EDL formation it drops the voltage to the equilibrium level of 0.5 V. As ions accumulate on the electrodes, this initially linear voltage distribution converges to a flat equilibrium profile. Depending on the analyzed points on the device the local voltage shows up and down shifts towards this equilibrium level. Note that the center of the device shows a flat response, this is because this point is already at the equilibrium condition. As a second step we probed the time response of the system. The results of the simulations are depicted in Fig. 6.

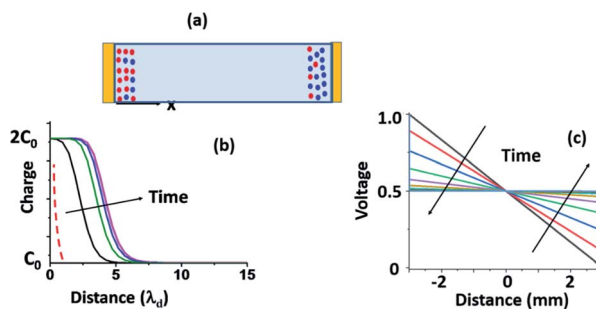


Fig. 6 Schematic representation of: (a) the ion distribution near both electrodes. (b) The ion distribution near the electrodes for the parallel plate capacitor and changes in the ion distribution near the electrified electrode as a function of time, after imposing a steric limit. Red dotted curve shows the voltage response in the absence of any steric limit. (c) Corresponding local voltage changes as a function of time along the perpendicular line to the plates.

As expected, the steric effects dramatically decrease the relaxation time of the capacitor from 200 to 2 ms, since the steric interactions significantly extend the width of the electric double layer and decrease the capacitance of the electrode surface. In the absence of a steric limit, the conventional Debye screening length is about  $\lambda = 0.1$  nm, but length scale and accumulated charge densities around the electrodes are not realistic. In our simulation, the finite size of the ion leads to the formation of a much larger condensed layer of  $\lambda > 1$  nm. This extension and the decrease in the capacitance eventually decrease the response of the system. The intuition behind this process can be simply grasped by analyzing a typical response time of a parallel plate capacitor which is defined by the  $RC$  time constant. Capacitance  $C$  is controlled by the electric double layer formation on the surfaces and resistance  $R$  is set by ion conduction across the device.

When we compare the experimental and simulation results of time responses, we find that the experimental results are much slower than can be predicted by the numerical calculations,  $\tau_{\text{exp}} = 4$  s  $\gg$   $\tau_{\text{sim}} = 2$  ms. Moreover, as we noted earlier, the other surprising feature we observed in XPS measurements is the extension of the voltage modulations deep into the electrode surfaces. These observations support the idea that 2-dimensional effects play a significant role in defining overall response of the system. Motivated by these observations and in order to account for these effects, we focused on simulating a more realistic configuration of the coplanar capacitor.

**(II-b) Simulations of charge dynamics of a co-planar capacitor.** The main difference between parallel and coplanar configurations is occurrence of time-dependent and non-uniform electric fields on the electrodes. To observe the

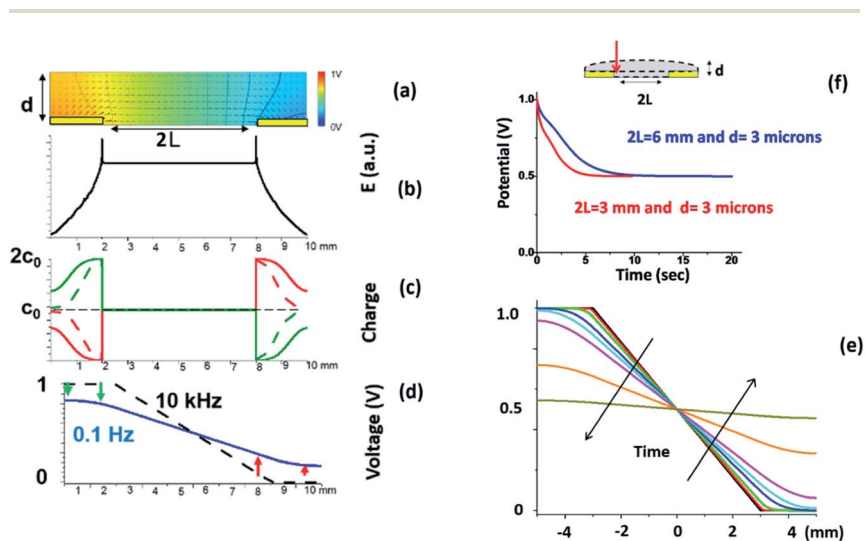


Fig. 7 (a) A schematic representation of 2D coplanar capacitor configuration, together with the color coded voltage profiles. (b) Magnitude of electric field on the surface of the electrodes under a suddenly applied voltage within 10 kHz and 0.1 Hz time-windows (*i.e.* 1/10 charging time). (c) Charge densities over the electrodes. (d) Voltage profiles at more frequencies. (e) Temporal variations of the extracted potential changes for the two devices near the electrified electrode as shown by the red arrow.

influence of this electric field profile on charge dynamics we performed 2-dimensional FEM simulations. Fig. 7 shows typical results of 2-dimensional cross-sectional view of electric field vectors, charge profiles and voltage distributions across the device. The magnitude of the electric field decays across the electrode surface. The main impact of this electric field profile is the emergence of a transient non-uniform electric double layer. Our simulations show that the drift of the charges and screening of the voltage on electrode surfaces significantly depend on the magnitude of the electric field. The non-uniform electric field eventually gives rise to non-uniform EDL layer formation across the surface of the electrodes. Due to steric effects the width of this condensed layer gradually grows.

In turn, the non-uniform and extended electrical double layer abruptly drops the electrode voltage and results also in a non-uniform voltage distribution. Although the double layer is buried under the IL film, the voltage profile on the electrodes can be measured on the surface of the IL droplet. This is simply observed by following the equipotential lines across the liquid film. Fig. 7(d) shows the simulated voltage profile on the droplet surface. This profile is dictated by the transient non-uniform EDL on electrode surfaces and can also be captured by XPS measurements. Moreover, the dynamics of this EDL can be monitored indirectly by measuring surface voltage. At a later stage, a non-uniform EDL gradually converges to a uniform distribution, and eventually reaches the equilibrium voltage across the device.

**(II-c) Effects of the device dimensions.** Through our simulation efforts, we have also noticed that the time response of the coplanar capacitor is particularly controlled by the thickness of the IL layer. This thickness together with the device length simply tunes the ion conduction of the system and sets the  $RC$  time

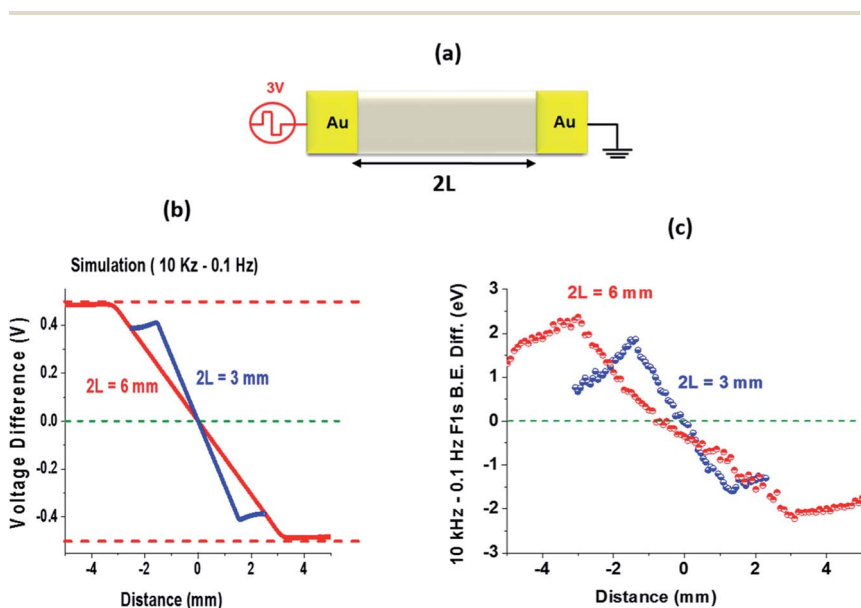


Fig. 8 (a) Schematics of the co-planar capacitor. Localized potential screening across the two co-planar capacitors obtained via: (b) simulations and (c) XPS measurements, for the two different devices, respectively.

constant. Our simulation results showed that a  $d = 3 \mu\text{m}$  thick and  $2L = 6 \text{ mm}$  long IL layer provides  $\tau_{\text{sim}} = 5 \text{ s}$  response time which is close to our experimental measurements. Moreover, for a similar but shorter device ( $2L = 3 \text{ mm}$ ) the same time constant is reduced to  $\sim 2.5 \text{ s}$ , again not too far off from the experimental data which are presented in Fig. 7(f) and 8.

The overall time constant of the device ( $\tau = RC$ ) can now be formulated to scale linearly with the device length and inversely with the ionic liquid film thickness ( $\tau \sim L/d$ ). This is in harmony with Bazant's predictions formulated for a parallel-plate capacitor, except for the very important finding that IL film thickness needs to be taken into account for 2-D ionic motion, as is the case for our coplanar capacitor.

## Conclusions

XPS under square-wave modulation is utilized to tap into the dynamics of localized charge accumulation and dissipation of a coplanar capacitor device, with an ionic liquid film as the electrolyte in between two gold electrodes in macro-dimensions. The results revealed two important findings: (i) dynamics of the charging/discharging processes are very slow, and (ii) temporal voltage variations are also measurable on electrode surfaces. In order to have deeper understanding, the COMSOL modelling software was used considering both 1- and 2-dimensional ionic motion. Simulation results were very successful in reproducing both temporal and spatial voltage variations across entire devices, measured by XPS. The simulation results also brought up a new understanding that the device time constant ( $\tau = RC$ ) is found to scale linearly with the device length and inversely with the ionic liquid film thickness ( $\tau \sim L/d$ ). This is in harmony with theoretical predictions, except for the new finding that IL film thickness has to be included.

## Conflicts of interest

There are no conflicts to declare.

## Acknowledgements

This work is supported by Grant No.: 118Z902 of the Scientific and Technological Research Council of Turkey (TUBITAK).

## References

- 1 R. Liu, S. Zhao and J. Liu, From Lithographically Patternable to Genetically Patternable Electronic Materials for Miniaturized, Scalable, and Soft Implantable Bioelectronics to Interface with Nervous and Cardiac Systems, *ACS Appl. Electron. Mater.*, 2021, **3**, 101–118.
- 2 C. Zhu, K. Huang, N. P. Siepser and L. A. Baker, Scanning Ion Conductance Microscopy, *Chem. Rev.*, 2021, **121**(19), 11726–11768.
- 3 Y. Tian, G. Zeng, A. Rutt, T. Shi, H. Kim, J. Wang, Y. Sun, B. Ouyang, T. Chen, Z. Lun, Z. Rong, K. Persson and G. Ceder, Promises and Challenges of Next-Generation “Beyond Li-ion” Batteries for Electric Vehicles and Grid Decarbonization, *Chem. Rev.*, 2021, **121**(3), 1623–1669.

- 4 K. Chen, D.-Y. Yang, G. Huang and X.-B. Zhang, Lithium–Air Batteries: Air-Electrochemistry and Anode Stabilization, *Acc. Chem. Res.*, 2021, **54**(3), 632–641.
- 5 B. Selvaraj, G. Shanmugam, S. Kamaraj, A. Gunasekeran and A. Sambandam, Effect of 1-Substituted 2-(Pyridin-2-yl)-1H-Benzo[d]imidazole Ligand-Coordinated Copper and Cobalt Complex Redox Electrolytes on Performance of Ru(II) Dye-Based Dye-Sensitized Solar Cells, *Inorg. Chem.*, 2021, **60**(3), 1937–1947.
- 6 A. Eftekhari, Supercapacitors utilising ionic liquids, *Energy Storage Mater.*, 2017, **9**, 47–69.
- 7 B. B. Hansen, *et al.*, Deep Eutectic Solvents: A Review of Fundamentals and Applications, *Chem. Rev.*, 2021, **121**(3), 1232–1285.
- 8 K. S. Egorova, E. G. Gordeev and V. P. Ananikov, Biological Activity of Ionic Liquids and Their Application in Pharmaceuticals and Medicine, *Chem. Rev.*, 2017, **117**(10), 7132–7189.
- 9 M. Watanabe, M. L. Thomas, S. Zhang, K. Ueno, T. Yasuda and K. Dokko, Application of Ionic Liquids to Energy Storage and Conversion Materials and Devices, *Chem. Rev.*, 2017, **117**(10), 7190–7239.
- 10 T. Welton, Ionic liquids: a brief history, *Biophys. Rev.*, 2018, **10**(3), 691–706.
- 11 A. J. Bard and L. R. Faulkner, *Electrochemical Methods: Fundamentals and Applications*, Wiley, 2000.
- 12 E. J. F. Dickinson and R. G. Compton, Influence of the diffuse double layer on steady-state voltammetry, *J. Electroanal. Chem.*, 2011, **661**(1), 198–212.
- 13 [https://en.wikipedia.org/wiki/Double\\_layer\\_\(surface\\_science\)](https://en.wikipedia.org/wiki/Double_layer_(surface_science)).
- 14 M. Z. Bazant, K. Thornton and A. Ajdari, Diffuse-charge dynamics in electrochemical systems, *Phys. Rev. E: Stat., Nonlinear, Soft Matter Phys.*, 2004, **70**(2), 021506.
- 15 M. S. Kilic, M. Z. Bazant and A. Ajdari, Steric effects in the dynamics of electrolytes at large applied voltages. I. Double-layer charging, *Phys. Rev. E: Stat., Nonlinear, Soft Matter Phys.*, 2007, **75**(2), 021502.
- 16 M. S. Kilic, M. Z. Bazant and A. Ajdari, Steric effects in the dynamics of electrolytes at large applied voltages. II. Modified Poisson-Nernst-Planck equations, *Phys. Rev. E: Stat., Nonlinear, Soft Matter Phys.*, 2007, **75**(2), 021503.
- 17 M. Z. Bazant, B. D. Storey and A. A. Kornyshev, Double Layer in Ionic Liquids: Overscreening versus Crowding, *Phys. Rev. Lett.*, 2011, **106**(4), 046102.
- 18 B. D. Storey and M. Z. Bazant, Effects of electrostatic correlations on electrokinetic phenomena, *Phys. Rev. E: Stat., Nonlinear, Soft Matter Phys.*, 2012, **86**(5), 056303.
- 19 M. V. Fedorov and A. A. Kornyshev, Ionic Liquids at Electrified Interfaces, *Chem. Rev.*, 2014, **114**(5), 2978–3036.
- 20 N. Gavish and A. Yochelis, Theory of Phase Separation and Polarization for Pure Ionic Liquids, *J. Phys. Chem. Lett.*, 2016, **7**, 1121–1126.
- 21 S. Bier, N. Gavish, H. Uecker and A. Yochelis, From bulk self assembly to electrical diffuse layer in a continuum approach for ionic liquids: the impact of anion and cation size asymmetry, *Phys. Rev. E*, 2017, **95**, 060201.
- 22 N. Gavish, D. Elad and A. Yochelis, From Solvent-Free to Dilute Electrolytes: Essential Components for a Continuum Theory, *J. Phys. Chem. Lett.*, 2018, **9**, 36–42.

- 23 V. Lockett, R. Sedev, J. Ralston, M. Horne and T. Rodopoulos, Differential Capacitance of the Electrical Double Layer in Imidazolium-Based Ionic Liquids: Influence of Potential, Cation Size, and Temperature, *J. Phys. Chem. C*, 2008, **112**(19), 7486–7495.
- 24 V. Lockett, M. Horne, R. Sedev, T. Rodopoulos and J. Ralston, Differential capacitance of the double layer at the electrode/ionic liquids interface, *Phys. Chem. Chem. Phys.*, 2010, **12**(39), 12499–12512.
- 25 M. Druschler, B. Huber and B. Roling, On Capacitive Processes at the Interface between 1-Ethyl-3-methylimidazolium tris(pentafluoroethyl) trifluorophosphate and Au(111), *J. Phys. Chem. C*, 2011, **115**, 6802–6808.
- 26 J. Zheng, S. S. Moganty, P. C. Goonetilleke, R. E. Baltus and D. Roy, A Comparative Study of the Electrochemical Characteristics of [Emim<sup>+</sup>][BF<sub>4</sub><sup>-</sup>] and [Bmim<sup>+</sup>][BF<sub>4</sub><sup>-</sup>] Ionic Liquids at the Surfaces of Carbon Nanotube and Glassy Carbon Electrodes, *J. Phys. Chem. C*, 2011, **115**(15), 7527–7537.
- 27 M. Jitvisate and J. R. T. Seddon, Direct Measurements of the Differential Capacitance of Solvent-Free and Dilute Ionic Liquids, *J. Phys. Chem. Lett.*, 2018, **9**, 126–131.
- 28 R. Hayes, N. Borisenko, M. K. Tam, P. C. Howlett, F. Endres and R. Atkin, Double Layer Structure of Ionic Liquids at the Au(111) Electrode Interface: An Atomic Force Microscopy Investigation, *J. Phys. Chem. C*, 2011, **115**(14), 6855–6863.
- 29 R. Atkin, N. Borisenko, M. Druschler, F. Endres, R. Hayes, B. Huber and B. Roling, Structure and dynamics of the interfacial layer between ionic liquids and electrode materials, *J. Mol. Liq.*, 2014, **192**, 44–54.
- 30 R. Hayes, G. G. Warr and R. Atkin, Structure and Nanostructure in Ionic Liquids, *Chem. Rev.*, 2015, **115**(13), 6357–6426.
- 31 I. Baylam, O. Balci, N. Kakenov, C. Kocabas and A. Sennaroglu, Femtosecond pulse generation with voltage-controlled graphene saturable absorber, *Opt. Lett.*, 2014, **39**, 5180.
- 32 A. Uysal, H. Zhou, G. Feng, S. S. Lee, S. Li, P. T. Cummings, P. F. Fulvio, S. Dai, J. K. McDonough, Y. Gogotsi and P. Fenter, Interfacial ionic ‘liquids’: connecting static and dynamic structures, *J. Phys.: Condens. Matter*, 2015, **27**(3), 032101.
- 33 M. Chu, M. Miller, T. Douglas and P. Dutta, Ultraslow Dynamics at a Charged Silicon–Ionic Liquid Interface Revealed by X-ray Reflectivity, *J. Phys. Chem. C*, 2017, **121**(7), 3841–3845.
- 34 D. Bedrov, J.-P. Piquemel, A. D. MacKerell, B. Roux and C. Schroder, Molecular Dynamics Simulations of Ionic Liquids and Electrolytes Using Polarizable Force Fields, *Chem. Rev.*, 2019, **119**(13), 7940–7995.
- 35 Y.-L. Wang, B. Li, S. Sarman, F. Mocci, Z.-Y. Lu, J. Yuan, A. Laaksonen and M. D. Fayer, Microstructural and Dynamical Heterogeneities in Ionic Liquids, *Chem. Rev.*, 2020, **120**(13), 5798–5877.
- 36 L. Collins, S. Jesse, J. I. Kilpatrick, A. Tselev, O. Varenky, M. B. Okatan, S. A. L. Weber, A. Kumar, N. Balke, S. V. Kalinin and B. J. Rodriguez, Probing charge screening dynamics and electrochemical processes at the solid–liquid interface with electrochemical force microscopy, *Nat. Commun.*, 2014, **5**(1), 3871.

- 37 L. Collins, J. I. Kilpatrick, S. V. Kalinin and B. J. Rodriguez, Towards nanoscale electrical measurements in liquid by advanced KPFM techniques: a review, *Rep. Prog. Phys.*, 2018, **81**(8), 086101.
- 38 M. A. Gebbie, M. Valtiner, X. Banquy, E. T. Fox, W. A. Henderson and J. N. Israelachvili, Ionic liquids behave as dilute electrolyte solutions, *Proc. Natl. Acad. Sci. U. S. A.*, 2013, **110**(24), 9674–9679.
- 39 M. A. Gebbie, A. M. Smith, H. A. Dobbs, A. A. Lee, G. G. Warr, X. Banquy, M. Valtiner, M. W. Rutland, J. N. Israelachvili, S. Perkin and R. Atkin, Long range electrostatic forces in ionic liquids, *Chem. Commun.*, 2017, **53**(7), 1214–1224.
- 40 A. A. Lee, C. S. Perez-Martinez, A. M. Smith and S. Perkin, Underscreening in concentrated electrolytes, *Faraday Discuss.*, 2017, **199**, 239–259.
- 41 L. Fillaud, T. Petenzi, J. Pallu, B. Piro, G. Mattana and V. Noel, Switchable Hydrogel-gated Organic Field-Effect Transistors, *Langmuir*, 2018, **34**, 3686–3693.
- 42 C. S. Perez-Martinez and S. Perkin, Surface forces generated by the action of electric fields across liquid films, *Soft Matter*, 2019, **15**, 4255–4265.
- 43 Y. Wang, R. Jarosova, G. M. Swain and G. J. Blanchard, Characterizing the Magnitude and Structure-Dependence of Free Charge Density Gradients in Room-Temperature Ionic Liquids, *Langmuir*, 2020, **36**, 3038–3045.
- 44 L. Richter, P. J. Zuk, P. Szymczak, J. Paczesny, K. M. Bak, T. Szymorski, P. Garstecki, H. A. Stone, R. Holyst and C. Drummond, Ions in an AC Electric Field: Strong Long-Range Repulsion between Oppositely Charged Surfaces, *Phys. Rev. Lett.*, 2020, **125**, 056001.
- 45 M. Han, H. Kim, C. Leal, M. Negrito, J. D. Batteas and R. M. Espinosa-Marzal, Insight into the Electrical Double Layer of Ionic Liquids Revealed through Its Temporal Evolution, *Adv. Mater. Interfaces*, 2020, **7**, 2001313.
- 46 D. Weingarh, A. Foelske-Schmitz, A. Wokaun and R. Kötz, In situ electrochemical XPS study of the Pt/[EMIM][BF<sub>4</sub>] system, *Electrochem. Commun.*, 2011, **13**(6), 619–622.
- 47 M. T. Camci, P. Aydogan, B. Ulgut, C. Kocabas and S. Suzer, XPS enables visualization of electrode potential screening in an ionic liquid medium with temporal- and lateral-resolution, *Phys. Chem. Chem. Phys.*, 2016, **18**(41), 28434–28440.
- 48 P. Aydogan Gokturk, B. Ulgut and S. Suzer, AC Electrowetting Modulation of Low-Volatile Liquids Probed by XPS: Dipolar vs. Ionic Screening, *Langmuir*, 2019, **35**(9), 3319–3326.
- 49 C. B. Uzundal, O. Sahin, P. Aydogan Gokturk, H. Wu, F. Mugele, B. Ulgut and S. Suzer, X-ray Photoelectron Spectroscopy with Electrical Modulation Can Be Used to Probe Electrical Properties of Liquids and Their Interfaces at Different Stages, *Langmuir*, 2019, **35**(52), 16989–16999.
- 50 P. Aydogan Gokturk, B. Ulgut and S. Suzer, DC Electrowetting of Nonaqueous Liquid Revisited by XPS, *Langmuir*, 2018, **34**(25), 7301–7308.
- 51 C. B. Uzundal, P. Aydogan Gokturk, S. Suzer and B. Ulgut, Coarse-Grained Electrostatic Model Including Ion-Pairing Equilibrium That Explains DC and AC X-ray Photoelectron Spectroscopy Measurements on Ionic Liquids, *J. Phys. Chem. C*, 2019, **123**(21), 13192–13200.
- 52 P. Aydogan Gokturk, M. Taner Camci and S. Suzer, Lab-based operando X-ray photoelectron spectroscopy for probing low-volatile liquids and their

- interfaces across a variety of electrosystems, *J. Vac. Sci. Technol., A*, 2020, **38**(4), 040805.
- 53 P. Aydogan Gokturk and S. Suzer, Probing dynamics of non-faradaic processes in ionic liquids at extended time and length scales using XPS with AC modulation, *J. Phys. Chem. C*, 2021, **125**, 9453–9460.
- 54 H. Zhao, Diffuse-charge-dynamics of ionic liquids in electrochemical systems, *Phys. Rev. E: Stat., Nonlinear, Soft Matter Phys.*, 2011, **84**, 051504.
- 55 R. F. Stout and A. S. Khair, Moderately nonlinear diffuse-charge dynamics under an ac voltage, *Phys. Rev. E: Stat., Nonlinear, Soft Matter Phys.*, 2015, **92**, 032305.
- 56 G. Feng, M. Chen, S. Bi, Z. A. H. Goodwin, E. B. Postnikov, N. Brilliantov, M. Urbakh and A. A. Kornyshev, Free and Bound States of Ions in Ionic Liquids, Conductivity, and Underscreening Paradox, *Phys. Rev. X*, 2019, **9**, 021024.
- 57 M. N. Huang, Y. Jiang, P. Saisanker, G. W. Driver and H. Weingartner, Static Relative Dielectric Permittivities of Ionic Liquids at 25 °C, *J. Chem. Eng. Data*, 2011, **56**, 1494–1499.
- 58 W.-L. Yuan, X. Yang, L. He, Y. Xue, S. Qin and G.-H. Tao, Viscosity, Conductivity, and Electrochemical Property of Dicyanamide Ionic Liquids, *Front. Chem.*, 2018, **6**, 59.